ЖЭТФ, 2002, том 121, вып. 1, стр. 73–87

THE GENERATION OF FAST PARTICLES IN PLASMAS CREATED BY LASER PULSES WITH DIFFERENT WAVELENGTHS

F. B. Rosmej, D. H. H. Hoffmann, W. Süß
Technische Universität Darmstadt, Institut für Kernphysik, Abt. Strahlen- und Kernphysik
D-64289, Darmstadt, Germany

A. E. Stepanov, Yu. A. Satov, Yu. B. Smakovskii, V. K. Roerich, S. V. Khomenko, K. N. Makarov, A. N. Starostin

Troitzk Institute of Innovative and Thermonuclear Research (TRINITI)
142092, Moscow, Russia

A. Ya. Faenov, I. Yu. Skobelev*, A. I. Magunov
Multicharged Ions Spectra Data Center of VNIIFTRI
141570, Mendeleevo, Moscow region, Russia

M. Geißel, P. Pirzadeh, W. Seelig
Technische Universität Darmstadt, Institut für Angewandte Physik
D-64289, Darmstadt, Germany

T. A. Pikuz
Bauman Moscow State Technical University
107005, Moscow, Russia

R. Bock
Gesellschaft für Schwerionenforschung, Plasmaphysics
D-64291, Darmstadt, Germany

T. Letardi, F. Flora, S. Bollanti, P. Di. Lazzaro
Dipartimento Innovazione, CR ENEA
Frascati, Italy

A. Reale, A. Scafati, G. Tomassetti
Dipartimento di Fisica e INFM, INFM g.e. LNGS, Università de L'Aquila
67010, L'Aquila, Italy

T. Auguste, P. d'Oliveira, S. Hulin, P. Monot
Centre d'Etudes de Saclay, DSM/DRECAM/SPAM
Bât 52291191, Gif-sur-Yvette, Cédex, France

B. Yu. Sharkov
Institute of Theoretical and Experimental Physics
117257, Moscow, Russia

Submitted 30 July 2001

PACS: 52.25.-b, 52.70.-m

*E-mail: skobelev@orc.ru

By means of spatially resolved high-resolution X-ray spectroscopy, we have investigated the generation of fast ions at various laser installations with different flux densities and laser wavelengths. It is demonstrated that the fast ion generation in laser-produced plasma can be achieved for a very low level of the averaged laser intensity onto the target. The time-of-flight mass spectrometry ion diagnostics and X-ray spectrographs give very close results for the energy distribution of the thermal ion component. For higher energies, however, we found significant differences: the spatially resolved high-resolution spectrographs expose the presence of supra-thermal ions, while the time-of-flight method does not. Supra-thermal ion energies E_{ion} plotted as a function of the $q\lambda^2$ parameter show a large scatter far above the experimental errors. The cause of these large scatters is attributed to a strong non-uniformity of the laser intensity distribution in the focal spot. The analyses by means of hydrodynamic and spectral simulations show that the X-ray emission spectrum is a complex convolution from different parts of plasma with strongly different electron density and temperature. It is shown that the highly resolved Li-like satellite spectrum near He_α contains significant distortions even for very low hot electron fractions. Non-Maxwellian spectroscopy allows determinating both the hot electron fraction and the bulk electron temperature.

1. INTRODUCTION

The interaction of intense laser radiation with matter leads to the creation of plasma in which the absorbed energy is not completely thermalized. This gives rise to the familiar phenomena of fast ion emission, understanding which is important for both the laser fusion and the development of fast ion sources [1–3].

Until now, the main part of the experimental information on the fast ion production in laser plasmas was obtained with the help of mass spectrometry methods (see, e.g., review [4] and the special issue [5]). These methods are based on the direct observation of ions over large distances, usually performed by charged particle detectors (e.g., Faraday detector) several meters away from the place of plasma creation. In this case, the results strongly depend on the recombination processes that occur during the plasma expansion to large distances. Thus, although these methods are suitable to investigate laser-produced plasmas as possible sources of multi-charged fast ions for some practical applications, they have serious limitations for studies of the fast ion production mechanisms inside the laser-produced plasma. More suitable for this purpose are the indirect spectroscopic methods — the observation of photons emitted by fast ions rather than the direct observation of fast ions. At present, such spectroscopic methods are not widely used for the investigations of fast ions. There are only several papers where these methods have been used in nanosecond [6–8] and femtosecond [9, 10] laser-produced plasmas.

In this paper, we present results for the fast ion production in plasmas created by nanosecond laser pulses with different wavelengths (0.308 μm, 0.8 μm, 1.06 μm, and 10.6 μm). The results of X-ray spectroscopic methods show that the parameter $q\lambda_{las}^2$ (where q is the laser flux density and λ_{las} is the laser wavelength) is important for the processes of fast ion generation but it does not completely determine these processes. It is also shown that using laser radiation with the wavelength ~ 1 μm, one can generate multicharged ions with the MeV energy (the so-called MeV-ions) even for moderate values of laser flux density at about 10^{13} W/cm^2.

2. EXPERIMENTAL SETUP

The experimental investigations were carried out at four different research centers: GSI-Darmstadt and the Technical University Darmstadt (Germany), Frascati (Italy), Saclay (France), and TRINITI (Russia). At GSI, the experiments were carried out at the «nhelix-laser» installation (nanosecond high energy laser for heavy ion experiments). «nhelix» is a Nd-Glass/Nd-Yag laser ($\lambda_{las} = 1.06$ μm) with the pulse duration 15 ns and the energy up to 100 J. The present experiments, however, were performed with the energy 17 J. The laser radiation is focused with a plane-convex lens (diameter 100 mm, focal length $f = 130$ mm) onto a solid teflon target (CF_2). With the spot size about 500 μm, we obtain the flux density about 10^{12} W/cm^2 onto the target and an extremely extended plasma source where the radiation emission of the He-like ions extends up to 1.5 cm [8]. In order to obtain different laser fluxes onto the target, the distance between the lens and the target was changed.

In the Saclay laser center, the experiments were performed with the UHI10, a Ti:Sapphire laser with $\lambda = 0.8$ μm. It was designed to generate 10 TW ultrashort pulses with a 10 Hz repetition rate. In the experiments reported here, the oscillator was switched off and

the amplified pulse was provided by a regenerative amplifier used as a free-running Q-switched nanosecond oscillator. The pulse had a nearly Gaussian temporal profile with the full width at half maximum equal to 8 ns. The available energy in the experimental chamber was between 0.6 and 0.8 J. The 80 mm diameter p-polarized laser beam was focused with an $f/2.35$ off-axis parabolic mirror onto a CF_2 target with the incidence angle $\phi_{las} = 45^\circ$ (Fig. 1). The $1/e^2$ focal spot radius was between 10 to 20 μm, giving the flux density about $5 \cdot 10^{13}$ W/cm^2.

The excimer laser HERCULES used in Frascati is a discharge pumped XeCl system ($\lambda_{las} = 0.308$ μm) designed and built by ENEA, INN FIS Department of Frascati [11]. The capacitor bank of HERCULES is directly connected with the laser electrodes. Just before the rising voltage reaches the self-breakdown level, an X-ray pulse is injected into the Ne-based XeCl gas mixture providing an avalanche process. This photo triggering technique allows circumventing the typical problem of a reliable switching in the main discharge circuit. In this way, HERCULES can be easily operated in the repetition rate mode without limitations because of both the high charge transfer ($\sim$ 30 mC) and the high current rate ($\sim 10^{11}$ A/s). In the present experiments, we used an injected PBUR (positive branch unstable resonator) configuration, which means that HERCULES was used as a laser amplifier amplifying the beam generated by a commercial laser (Spectra Physics) with a 10 ns pulse duration. The energy thus obtained was 2 J per pulse with the 10 Hz repetition rate. The laser beam was focused by a triplet lens (with the f-number $F = 3$) to a spot with the diameter 50–80 μm onto a plane solid target, giving the intensity about $6 \cdot 10^{12}$ W/cm^2.

In TRINITI, the experiments were carried out using the TIR-1 facility, which was thoroughly described in [12]. The TIR-1 scheme can be used to generate CO_2 laser pulses with stable parameters and duration that can be varied in the range from 2 to 30 ns. Gas-phase saturable absorbers eliminated the feedback between the target under study and the laser system. The wave front of the radiation was shaped by spatial filters and matched irises. The output beam with the diameter 200 mm had a divergence close to the diffraction limit. The laser system characteristics ensured good repeatability and optimization of the laser pulse parameters from the start. In the experiments described below, the laser source was a single-mode CO_2 oscillator built around the amplifier module of the TIR-1 facility with the active volume $\sim$ 17 liters. The radiation was produced in an unstable resonator with the length 2.7 m and the amplification $\sim$ 3. The energy of the output beam with the diameter 150 mm was about 60 J, and the laser pulse duration was 20 ns. The laser radiation is focused with a lens (with the focal length $f = 600$ mm) onto a solid magnesium target with the spot diameter about 500 μm. In this case, the laser flux density was about 10^{12} W/cm^2. In order to obtain different laser fluxes onto the target, the distance between the lens and the target was varied.

In all experiments, soft X-ray radiation was simultaneously recorded by two spectrographs with spherically bent mica crystals. The angle between the target normal and the laser beam was ϕ_{las}, and the angle between the target surface and the central ray of the second (b) spectrograph was ϕ_b. The curvature radii of the crystals were 150 mm and 100 mm. Both spectrographs were installed in the FSSR-2D scheme [13, 14]. This allowed observing spectra with the spectral resolution $\lambda/\delta\lambda = 3000$–$5000$ and spatial resolution $\delta x = 25$–45 μm. In the TRINITI experiments, we simultaneously used both the X-ray spectroscopy and traditional mass spectrometry (described in detail in [12]) diagnostics.

The experiments at GSI, Frascati and Saclay were performed with flat solid teflon targets. In these cases, spectrographs were tuned to the spectral region 13.7–17 Å containing the resonance line Ly_α of H-like F IX and the lines He_α, He_β, and He_γ of He-like F VIII. In the TRINITI experiments, flat solid magnesium targets were used. In this case, we observed (in the second order of crystal reflection) the spectral regions 9.0–9.5 Å and 7.8–8.6 Å, which contain the Ly_α line of Mg XII and the He_α and He_β lines of Mg XI. Examples of the spectrograms and densitograms obtained are presented in Figs. 1–2.

3. RESULTS AND DISCUSSION

The main idea to use the X-ray spectroscopy for the observation of fast ions is as follows. Suppose that a plasma expansion predominantly occurs in the direction normal to the target surface (the z axis). The observed emission spectra then depend on the angle between the direction of observation and z axis because of the Doppler effect. Using several spectrographs simultaneously, it is possible to derive the direction of the predominant plasma expansion and its velocity distribution from the observed spectra. For example, if the plasma is cylindrically symmetric (the usual case for the interaction of a laser pulse with a flat target) the use of two spectrographs already provides the necessary

Fig. 1. The X-ray images of fluorine (a) and densitograms (b) obtained from the teflon plasma radiation for different observation directions: *1* — parallel to the target surface, *2* — at the angle $\phi_b = 45^\circ$ to the target surface ($\phi_{las} = 0$). The XeCl laser pulse parameters are $\lambda_{las} = 0.308$ μm, $\tau_{las} = 12$ ns, $E_{las} = 2$ J, $q = 6 \cdot 10^{12}$ W/cm^2, and $q\lambda_{las}^2 = 6 \cdot 10^{11}$ W·μm^2/cm^2

information. In this case, spectrograph (a) observes the plasma in the direction perpendicular to the z axis and the line profiles are expected to be essentially symmetric. The width of the lines (apart from the random walk characterized by the ion temperature T_i) is determined by the transverse component $V_{x,y}$ of the plasma expansion velocity,

$$\frac{\Delta\lambda(a)}{\lambda} \approx \frac{V_{x,y}}{c}. \tag{1}$$

For the second spectrograph (b), the situation is different: the plasma motion is not symmetric, because the plasma moves only in the positive z direction. The spectral line is then shifted to shorter wavelengths by

$$\Delta\lambda = \lambda_0 \frac{V_z}{c} \sin\phi_b. \tag{2}$$

Because different ions can have different expansion velocities, the observed spectra show corresponding wings on the blue side of all spectral lines. The line profile is strongly asymmetric. Using the relation

$$I\left(\lambda_0 + \lambda_0 \frac{V_z}{c} \sin\varphi_b\right) \propto N(V_z), \tag{3}$$

it is possible to determine the number $N(V_z)$ of fast ions for a given velocity, i.e., the velocity distribution. We note that usually $V_z \gg V_{x,y}$, and consequently, the asymmetry observed by spectrograph (b) must be much more pronounced than the broadening observed by spectrograph (a). Exceptions from the symmetrical line shape for spectrograph (a) can be caused by radiation transport effects in transverse differentially moving (x-, y-direction) plasmas. Differential plasma motion results in a relative shift of the emission and absorption profiles and the emission profiles are asymmetric [2].

The first X-ray spectroscopic observations of fast ions in a laser-produced plasma from solid targets were made many years ago [6, 7]. The spectral distribution of the Doppler-shifted radiation from fast He-like ions was detected using flat or cylindrically bent crystal spectrographs. This technique has the serious drawback of spatial integration (we note that although the introduction of slits in principle also provides a spatial resolution with flat crystals, the intensity considerably drops and the signal-to-noise ratio becomes insufficient for a detailed analysis of spectra). However, the use of focusing spectrographs with spherically bent crystals allows obtaining a high spatial resolution while maintaining high luminosity. The high spectral and spatial resolution as well as the high luminosity allow measure-

Fig. 2. The X-ray images of fluorine (a) and densitograms (b) obtained from the teflon plasma radiation for different observation directions: *1* — parallel to the target surface, *2* — at the angle $\phi_b = 90^\circ$ to the target surface ($\phi_{las} = 45^\circ$). The Ti:Sapphire laser pulse parameters are $\lambda_{las} = 0.8$ μm, $\tau_{las} = 8$ ns, $E_{las} = 0.7$ J, $q = 5 \cdot 10^{13}$ W/cm^2, and $q\lambda_{las}^2 = 3 \cdot 10^{13}$ W·μm^2/cm^2

ments for low intensity sources (and less intense lines, which are extremely important for diagnostic purposes) with higher spectral line densities.

The spectrograms shown in Figs. 1 and 2 were obtained using the various laser facilities described above. Figure 1 presents the plasma production by a relatively low-intensity and short-wavelength laser pulse. Figure 1*a* shows the images and Fig. 1*b* shows the corresponding traces (spectra). The lines from highly charged fluorine detected by the spectrometer aligned perpendicularly to the plasma expansion axis, i.e., along the target surface (images *1* in Fig. 1*a*) exhibit a symmetrical shape. The width of the He_α and He_β lines are approximately equal to each other, indicating that Stark broadening does not dominate in the line wings. Images *2* in Fig. 1*a* correspond to aligning the spectrograph at the angle $\phi_b = 45^\circ$ to the target surface. More details are seen from the spectra obtained by tracing the corresponding images, Fig. 1*b*, spectra *1* and *2*. The width of the lines is determined by the Doppler broadening due to the expansion at thermal velocities and by the plasma optical thickness.

In contrast, the results obtained for the teflon plasma using the GSI and Saclay laser facilities (see, e.g., Fig. 2) show that the line shape detected in the direction at 55° to the target surface exhibits a strong asymmetry in the blue wings (e.g., for each line He_α, He_β, He_γ, Ly_α). This asymmetry occurs because of the expansion dynamics and corresponds to large Doppler shifts (which cannot be explained by thermal expansion) and manifests the existence of a considerable amount of fast ions. The arrow near the curve in Fig. 2*b* shows the value of the Doppler shift that corresponds to the relative velocity $5 \cdot 10^8$ cm/s. We note that although the laser wavelengths and pulse durations were rather similar, the pulse energies and focusing conditions were quite different.

Similar results were obtained for the Mg plasma produced by the long-wavelength CO_2-laser pulse for the observation angle $\phi_b = 45^\circ$. In this case, the line asymmetry is pronounced for the optically thick resonance line ($He_{\alpha 1}$) and for the spectrally resolved optically thin intercombination line ($He_{\alpha 2}$).

The extraction of the average energy of fast ions

from the measured spectra is based on the analysis of the blue wings of the spectral lines. Because the motion of ions is directed towards the spectrograph, the radiation emitted by fast ions must not pass through dense absorbing plasma regions. We now estimate possible absorption effects. The frequency-dependent optical thickness is given by

$$\tau_{ji}(\omega) = \int_0^L \frac{1}{4}\lambda_{ji}^2 \frac{g_j}{g_i} A_{ji} n_i \varphi_{ji}(\omega) dx, \qquad (4)$$

where λ_{ji} is the wavelength for the transition $j \to i$, g_j and g_i are the statistical weights of the upper/lower states, A_{ji} is the spontaneous transition probability, n_i is the absorbing ground state, ϕ_{ij} is the line profile, and L is the relevant plasma size. The line center optical thickness τ_0 can be estimated from

$$\tau_{0,ji} \approx 1.25 \cdot 10^{-10} \lambda_{ji}^3[\mathrm{m}] \times \\ \times A_{ji} \frac{\lambda}{\Delta\lambda} n_i[\mathrm{cm}^{-3}] L_{eff}[\mu\mathrm{m}], \qquad (5)$$

where $\lambda/\Delta\lambda$ is the relative line width. For a Doppler profile, the relative line width is given by

$$\frac{\Delta\lambda}{\lambda} = 7.69 \cdot 10^{-5} \sqrt{\frac{kT_i[\mathrm{eV}]}{M[\mathrm{amu}]}}\,. \qquad (6)$$

For $n_e = 10^{21}$ cm^{-3} (the critical density of the Nd-Glass laser), $kT_i = 200$ eV, $M = 24$, and $L_{eff} = 100$ μm, we obtain $\tau_0 \approx 40$ for the He-like resonance line $\mathrm{He}_{\alpha 1}$ of Mg ($A = 1.95 \cdot 10^{13}$ s^{-1}) and $\tau_0 \approx 0.1$ for the intercombination line $\mathrm{He}_{\alpha 2}$ ($A = 3.40 \cdot 10^{10}$ s^{-1}). The optical thickness of the intercombination line can therefore be neglected even in the line center and for the resonance line, the optical thickness is negligible about one FWHM out of the line center. Therefore, the spectral dependence of the intensities is directly related to the ion velocity distribution function.

Figure 3 shows the relative intensity in the blue wings of the He_β line of fluorine versus the Doppler shift measured in terms of the ion energy (directed motion). The smooth lines represent Maxwell distribution fits (with the temperature determined by the angle to the abscissa axis in logarithmic plots). The results show that the experimental uncertainty is sufficiently small to determine the average energy values for the fast ions. It should be noted that the difference between the Saclay (Fig. 3*a*) and GSI (Fig. 3*b*) results can be caused by two reasons. The first is the higher laser flux density for UHI10 facility. The second reason can be related to a resonance absorption of the

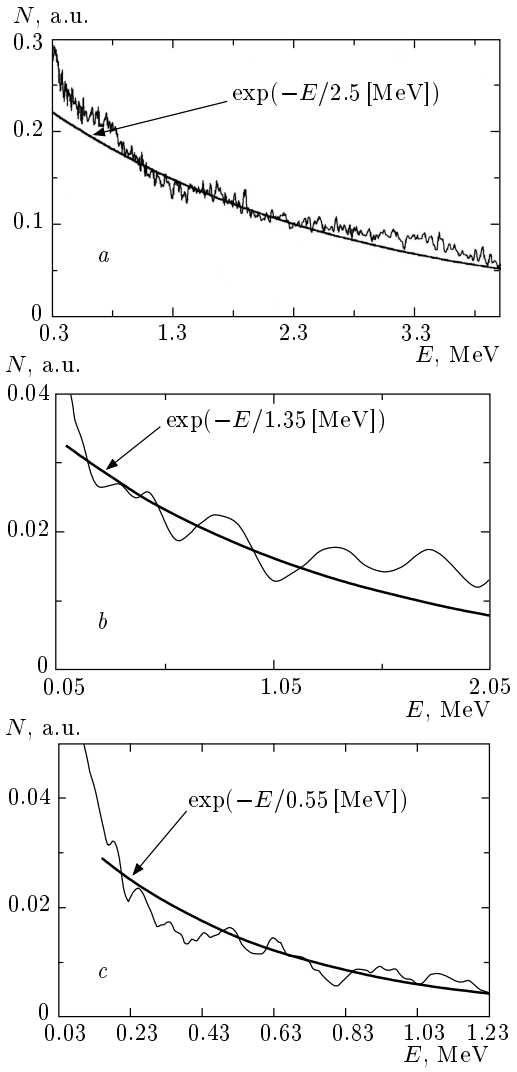

Fig. 3. Ion energy distributions derived from the relative intensities in the blue wings of the spectral lines of He_α of F VIII and He_α of Mg XI. The smooth lines represent the Maxwell distribution fits: *a* — Saclay experiment, *b* — GSI experiment, *c* — TRINITI experiment

p-polarized laser pulse [15–17] occurring when the angle $\phi_{las} \neq 0$. Figure 3*c* shows the results for the TIR-1 CO_2-laser installation.

Figure 4*a* presents the velocity distribution of He-like ions measured in the TRINITI experiment (CO_2 Laser) by the mass spectrometer. Figure 4*b* shows the mass spectroscopic measurements together with the line spectroscopic results obtained from the He-like Mg lines. The low-velocity part is obtained from the optically thin He-like intercombination line

$$\mathrm{He}_{\alpha 2} = 1s2p\,^3P_1 \to 1s^2\,^1S_0 + h\nu,$$

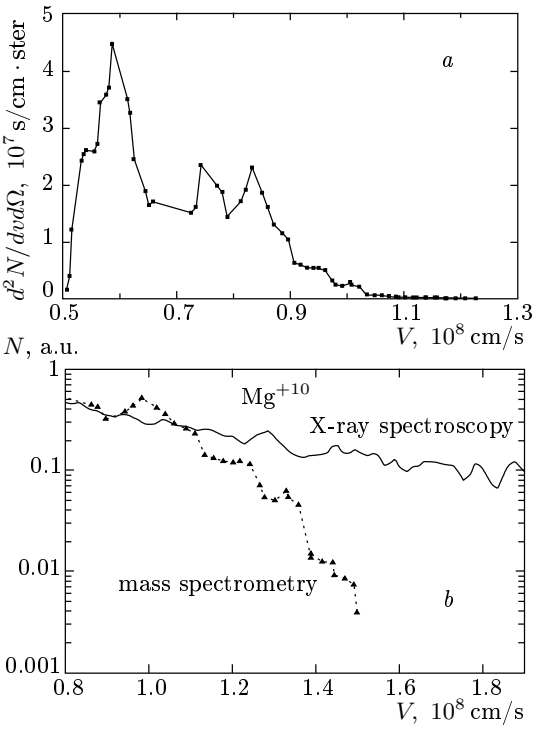

Fig. 4. *a* — Mass spectroscopic measurements of the He-like Mg ion velocity distribution in CO_2 laser-produced plasmas; *b* — comparison of the Mg XI ion velocity distribution in the CO_2 laser plasma derived from the X-ray spectroscopy (solid line) and mass spectrometry (dotted line with symbols) methods

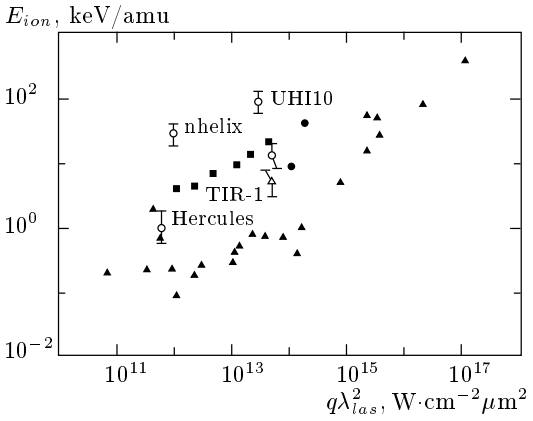

Fig. 5. The average fast ion energy E_{ion} [keV/amu] vs. $q\lambda^2_{las}$. Open symbols are the results obtained in the present work: circles are the X-ray spectroscopy measurements, the triangle is the mass spectrometry measurement. The filled circle is the X-ray spectroscopic result from [6], filled triangles denote the data in [15–24] and filled squares are the results in [15, 17]

whereas the high-velocity part originates from the He-like resonance line

$$\mathrm{He}_{\alpha 1} = 1s2p\,{}^1P_1 \to 1s^2\,{}^1S_0 + h\nu.$$

It can be seen that for velocities below $1.4 \cdot 10^8$ cm/s (with $1.4{\cdot}10^8$ cm/s corresponding to the energy 245 keV for Mg ions), the agreement is very good, however, only the line spectroscopic measurements access the higher-velocity region.

Figure 5 presents the fast ion average energy per nucleon as a function of the parameter $q\lambda^2_{las}$ as was proposed in [4]. In Fig. 5, we compare the measurements carried out for flat targets and ns-laser pulses [6, 7, 18–25]; we note, however, that the measurements indicated with filled squares were obtained for 35 ps-pulses [15, 17]. The results of the present mass-spectrometry measurements (open triangles in Fig. 5) are also shown. The various results show a large scattering (by orders of magnitude) of the data for both the X-ray observations and the mass spectroscopy measurements. This indicates that the parameter $q\lambda^2_{las}$ may not be the only important parameter in the description of the fast ion generation.

We note that the mass-spectrometry and the X-ray spectroscopy methods deal with different registration areas. In the first method, the ions are detected in the region far from the laser pulse and the interaction zone, while in the second method, the interaction region involves the various processes related to the formation of the spontaneous X-ray radiation. One can therefore expect a more complicated scaling behavior of the average energy with the laser pulse parameters than presented in [4]. At the same time, the direct measurements from the interaction region provide more information for the understanding of the fast ion generation mechanisms.

4. SIMULATION TECHNIQUES

To reveal the physical phenomena responsible for different features of the measured X-ray spectra, we performed numerical simulations using two computer codes. The first is the one-dimensional GIDRA-1 code for the simulation of plasma hydrodynamics and population kinetics. Although the real plasma movement is evidently not one-dimensional, this approach allows obtaining a good estimate of the average plasma parameters. The numerical model is described in detail in [26]. Plasma hydrodynamics is described in the one-fluid two-temperature approximation. The model includes the electron heat conduction with the heat flux limi-

tation, electron-ion temperature relaxation, and heating by laser light taken into account semi-empirically. The electron energy balance equation also includes terms corresponding to the ionization and excitation of plasma ions and to the energy loss due to the plasma radiation. The energy losses due to the radiation in spectral lines and in the continuum are self-consistently taken into account along with the hydrodynamics and population kinetics. The interaction of laser light with plasma is modelled in the geometrical optics approximation by the ray-tracing technique. The ideal gas equation of state was used to couple the system of equations.

The total amount of atomic and ionic states for Mg used in simulation was 77. The atomic model equations were solved self-consistently along with the hydrodynamics equations, which also allowed correctly treating the transient effects in population kinetics. Temperature-dependent rates are calculated under the assumption that the temperature distribution of electron energies obtained from hydrodynamics is given by the Maxwell distribution function. The effect of the line radiation re-absorption was described within the photon escape probability approach. The values of escape probabilities were calculated in the Sobolev approximation [27]. The drawback of the GIDRA-1 code for the purpose of X-ray spectra analysis is that the doubly excited states are absent in the atomic model, and no satellite lines are therefore present in the generated spectrum.

On the other hand, another code package exploited in the course of present work, MARIA [28], solves multilevel multiion stage atomic model equations with two important features: the correct account for a large number of doubly excited levels and a non-Maxwellian electron energy distribution function. MARIA solves the completely transient set of nonlinear population kinetics equations

$$\frac{dn_j}{dt} = -n_j \sum_{k=1}^{N} W_{jk} + \sum_{i=1}^{N} n_i W_{ij}, \tag{7}$$

where n_j are the population densities, N is the maximum number (dynamic) of levels (ground, singly- and multi-excited states of various ion stages), and the W matrix contains all the collision radiative processes and radiation transport effects. If a matrix element physically does not exist, its value is zero. More details related to the applications to spectra interpretation are described elsewhere [2, 28–31].

We have confined ourselves to the representation of non-Maxwellian distribution functions with the lowest possible number of «temperature parameters T» that allowed achieving a reasonable description of the experimental spectra. This was checked by means of three T parameters and a mono-energetic beam by changing the respective relative fractions and energies. The non-Maxwellian electron distribution function can then be characterized by the hot electron fraction

$$f_{hot} = \frac{n_{hot}}{n_{cold} + n_{hot}}. \tag{8}$$

The non-Maxwellian rate coefficients are given by

$$\langle V\sigma\rangle = (1 - f_{hot})\langle V\sigma, T_{cold}\rangle + f_{hot}\langle V\sigma, T_{hot}\rangle, \tag{9}$$

where the brackets indicate the integration of the cross-section with the distribution function (assumed to be Maxwellian with the parameter T),

$$\langle V\sigma, T\rangle = \int_{E_0}^{\infty} \sigma(E)V(E)F(E)dE, \tag{10}$$

where

$$F(E) = \frac{2}{\sqrt{\pi}}\sqrt{E}\,\frac{\exp(-E/kT)}{(kT)^{3/2}}. \tag{11}$$

For the three-body recombination, the corresponding expression is more complicated because it then becomes necessary to simultaneously introduce two distribution functions and the double differential ionization cross section

$$\langle V\sigma^{Tr}\rangle = (1 - f_{hot})^2\langle V_1V_1\sigma^{Tr}\rangle + f_{hot}^2\langle V_2V_2\sigma^{Tr}\rangle + 2f_{hot}(1 - f_{hot})\langle V_1V_2\sigma^{Tr}\rangle, \tag{12}$$

where

$$\langle V_kV_l\sigma_{ji}^{Tr}\rangle = \frac{\pi^2\hbar^3}{m_e^2}\frac{g_i}{g_j}\int_0^{\infty} dE_k \times \times \int_0^{\infty} dE_l \frac{E}{\sqrt{E_kE_l}}\,\sigma_{ij}^{I}(E, E_k)F(E_k)F(E_l). \tag{13}$$

If $k = l$, the integral in Eq. (13) can be reduced to an integral involving the usual ionization cross section $\sigma^I(E)$ (physically, this is equivalent to the application of the detailed balance principle). For $k \neq l$, the integrals are calculated numerically using the double differential ionization cross section $\sigma_{ij}^I(E, E_k)$.

Because we use the MARIA code to generate the detailed X-ray spectra either for given plasma density, temperature and electron distribution function, we first investigated the validity of this approach. The two important features of laser plasma are the strong non-uniformity of plasma parameters and the essentially

transient ionization and recombination processes occurring when plasma flows from the cold nearly solid-state density region through the hot critical zone to the rare and rather cold «corona». We restrict our treatment to one-dimensional effects (however, spherical geometry was chosen).

One type of simulations was made for a Nd laser at the irradiation conditions corresponding to the experiments at the «nhelix-laser» facility at GSI. The target was assumed to be solid magnesium. The pulse shape was Gaussian with the FWHM 15 ns, the peak of the pulse was shifted by 7.5 ns from the start of the simulation (therefore, the simulation time $t = 7.5$ ns corresponds to the peak of laser power). The peak power density of a pulse with the Gaussian temporal shape irradiating a solid target was set as $P_{las} = 10^{12}$ W/cm^2, $\lambda = 1.06$ μm. The initial radius of the target was set to $R_0 = 750$ μm.

Figure 6 presents the results of this simulation for a (Lagrangian) plasma particle that passes the point where T_e reaches the maximum at the time of the laser power peak. Figure 6*a* shows the relative abundances of Li-like and He-like Mg as a function of time for the Lagrangian particle. It is clearly seen that Li-like ions are present only for a few nanoseconds. Thereafter, the He-like ion population becomes dominant very soon. After the electron density becomes several times smaller than the critical density, the ionization state of the plasma becomes «frozen» because the characteristic recombination time is much longer than the characteristic time of rarefaction. For the same Lagrangian particle, we also calculated the relative abundances obtained under the assumption that all populations are in a steady state. The steady-state He-like ion population becomes significantly different from the transient one only after 15 ns when the laser pulse is already over. Figure 6*b* shows the evolution of the electron density N_e and the electron temperature T_e. In Fig. 6*c*, the radiation power loss per unit volume is plotted for the resonance line of He-like Mg ions. The peak of the radiation power loss occurs slightly earlier than the peak of the electron temperature. This is because the electron density is rapidly decreasing.

Another type of GIDRA-1 simulations corresponds to irradiation conditions at the TIR-1 laser facility at TRINITI. The initial radius was set to $R_0 = 200$ μm. The optical system of the TIR-1 laser was designed to provide power density close to 10^{14} W/cm^2. However, it turned out to be impossible to obtain high-quality spectra because of film over-exposure (probably caused by fast electrons hitting the crystal and resulting in the X-ray radiation from the mica surface). To avoid this

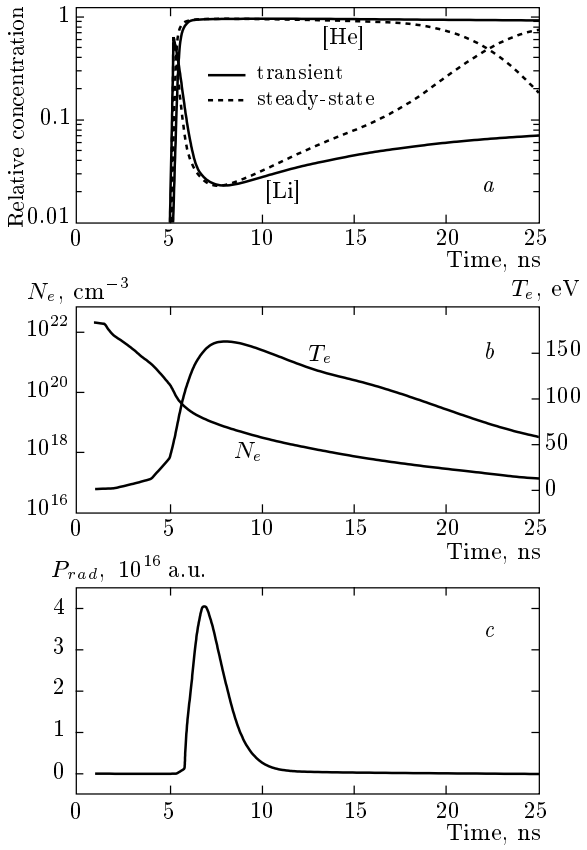

Fig. 6. Hydro-simulation for the Nd glass laser (GSI), $P_{las} = 10^{12}$ W/cm^2, $\lambda = 1.06$ μm, the initial target radius $R_0 = 750$ μm, the full Gaussian width $\tau = 15$ ns. Shown are the relative ion abundances (*a*), temperature and density (*b*), and radiation output of the He-like resonance line (*c*)

effect, the target was displaced from the optimal focus position. This led to a smaller laser power density and significantly decreased the amount of fast electrons. In accordance with estimates, the peak intensity in the simulation was set to $P_0 = 2 \cdot 10^{12}$ W/cm^2. The pulse shape was Gaussian with the full width at half maximum equal to 26 ns, the peak of the pulse was shifted by 13 ns from the start of the simulation. Simulations were performed in spherical geometry providing a qualitatively correct distribution of plasma parameters even for the one-beam illumination geometry of a plane target (provided the initial diameter of the target in the simulation is about 1.5-2 times larger than the focal spot size). The initial radius of the spherical target for the simulation was 400 μm, while the focal spot size in the experiment is estimated to be 400–600 μm.

Simulation data are shown in Fig. 7. Because the peak of the electron temperature is higher than it was

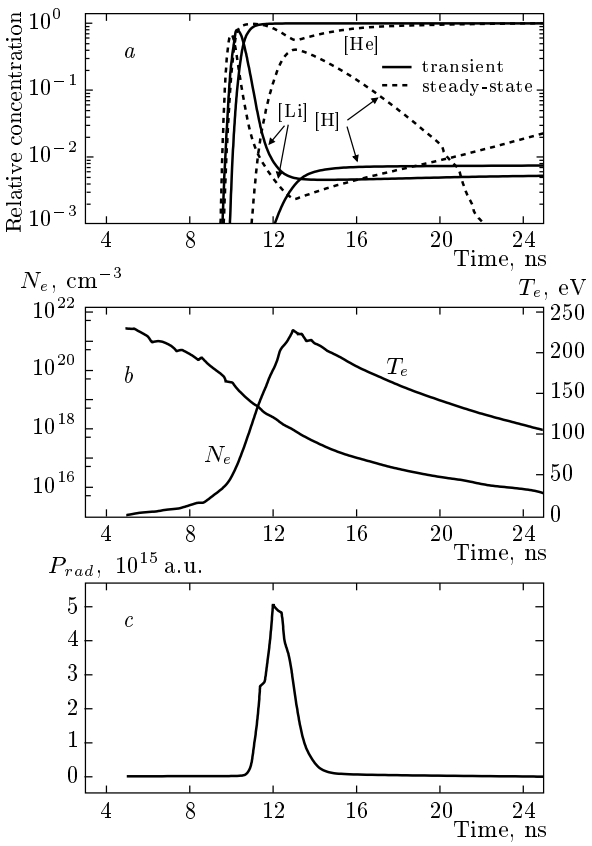

Fig. 7. Hydro-simulation for the CO_2 laser (TRINITI), $P_{las} = 6 \cdot 10^{12}$ W/cm^2, $\lambda = 10.6$ μm, the initial target radius $R_0 = 200$ μm, the full Gaussian width $\tau = 26$ ns. Shown are the relative ion abundances (a), temperature and density (b), and radiation output of the He-like resonance line (c)

in the Nd glass laser simulation, stationary populations deviate from the transient values at the temperature peak moments. The strongest effect is observed for the H-like ions: the relative abundance is less than 1% in the transient simulation, but 2 orders of magnitude larger in the steady-state simulation. The intensity peak of the He-like resonance line occurs before the temperature peaks (deviations of stationary populations from the transient ones are small). Based on these results, we expect that X-ray spectra produced by the MARIA code are reasonably accurate for the plasma regions close to the target surface.

5. INVESTIGATION OF HOT ELECTRONS

Theoretical models [4, 15, 17] relate the generation of fast ions to the appearance of hot electrons. Although various mechanisms are under discussion (e.g., [4, 15, 17, 32, 33]), a satisfactory understanding is still missing. In this situation, the experimental investigation of fast ions and hot electrons inside the plasma volume where the laser energy is absorbed is mandatory for the understanding and benchmarking of theoretical models. X-ray spectroscopy set up with a high spectral and spatial resolution proves to be an excellent tool for these purposes. Moreover, the development of models for the interpretation of non-Maxwellian emission spectra have shown that the radiation from autoionizing states (the so-called dielectronic satellite spectra) play a significant role [8, 28–30, 34–40]. However, the registration of these important satellite transitions requires very high-luminosity spectrographs. Spherically bent mica crystals [13, 14] have been proved to simultaneously satisfy all the requirements that are necessary in practical applications: high spectral resolution ($\lambda/\delta\lambda \approx 5.000$), high spatial resolution ($\delta x \approx 10$ μm), high luminosity, and a sufficiently large spectral interval for the registration of various line emissions.

Figure 8a shows the spectral interval from the He-like intercombination line up to the Li-like kj-satellites (see, e.g., [41] for the satellite designation) from the nhelix-Nd-Glass/YAG-laser at GSI. The spectrum corresponds to the distance about 1.9 mm from the center of the laser spot. For these areas, the laser flux density is much lower than for the central spot and we do not expect a considerable amount of hot electrons and fast ions. This spectrum is therefore suitable to experimentally cross-checking the spectra simulations of multi-excited ions under well-defined conditions. The theoretical modelling (thick line in Fig. 8a) fits the experiment in all spectral details with the following parameters: the electron temperature $kT_e = 200$ eV, the electron density $n_e = 2 \cdot 10^{20}$ cm^{-3} and the photon path length $L_{eff} = 500$ μm. The essential point here consists in the simultaneous match of the intercombination line $He_{\alpha 2}$, the qr-, a-d-, and jk-satellites that strongly depend on non-Maxwellian electrons because of their different excitation channels and excitation mechanisms [8, 28, 36]. It can be clearly seen that a good modelling is obtained without the introduction of hot electrons (we note that the slight discrepancies in wavelengths are not caused by inaccurate atomic data but rather by a nonlinear experimental wavelength scale). It is also worth paying attention to the good interpretation near the intercombination line $He_{\alpha 2}$: first, we note that no blue wings are observed, and second, we also obtained a good agreement of the satellite structure near the positions indicated with «nm» and «st». In fact, the corresponding intensities are caused by the emission not only from the Li-like $1s2l2l'$-satellites nm/st but

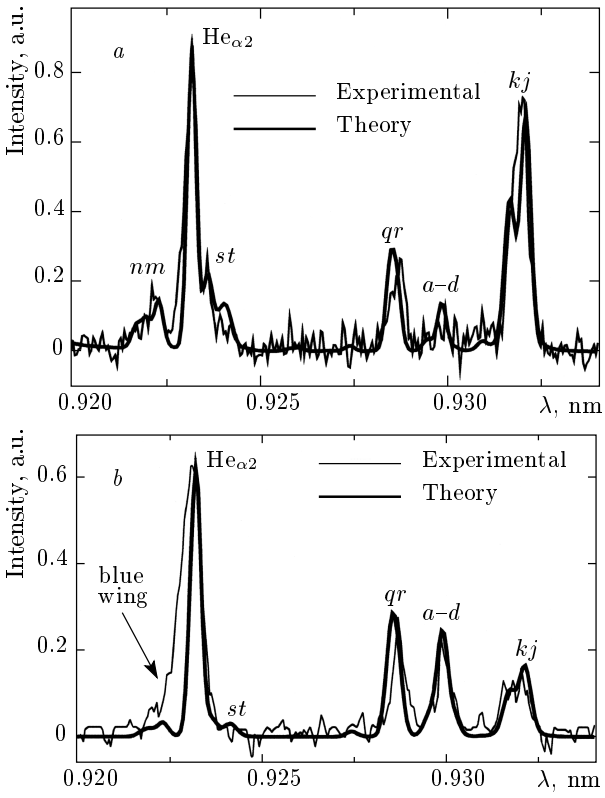

Fig. 8. *a* — Experimental spectrum from the ns-nhelix laser at GSI. A good match between the theory (thick curve) and the experiment (thin curve) is obtained for the plasma parameters $kT_e = 200$ eV, $n_e = 2 \cdot 10^{20}$ cm^{-3}, $L_{eff} = 500$ μm; *b* — experimental spectrum from He- and Li-like Mg ions obtained from the TRINITI CO_2 laser at 320 μm from the central spot. A good agreement could only be obtained assuming a non-Maxwellian energy distribution function. The simulation parameters are: $kT_{cold} = 60$ eV, $n_e = 1 \cdot 10^{19}$ cm^{-3}, $kT_{hot} = 1$ keV, $f_{hot} = 4 \cdot 10^{-7}$, and $L_{eff} = 500$ μm.

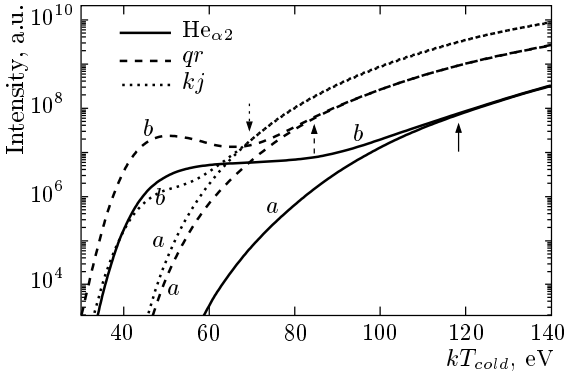

Fig. 9. Intensities of the He-like intercombination line $He_{\alpha 2}$ and the Li-like satellites qr and jk for different values of T_{cold} and different fractions of hot electrons: $n_e = 10^{21}$ cm^{-3}, $kT_{hot} = 2$ keV. The arrows indicate the different threshold values of kT_{cold} for the strong onset of the hot electron influence on the line emission; $f = 0$ (*a*), 10^{-5} (*b*)

also from higher-order satellites originating from the $1s2lnl'$-configurations. Extended atomic data calculations and subsequent spectra simulations have shown that these higher-order satellites accumulate not only near the He-like resonance line $He_{\alpha 1}$, but also near the He-like intercombination line $He_{\alpha 2}$ [30].

An entirely different situation is realized for CO_2 laser-produced plasmas. Figure 8*b* shows the emission spectrum obtained from the TRINITI installation. Numerous parameter variations showed that the experimental situation could not be fitted by simulations with a Maxwellian electron energy distribution function. We have also investigated highly transient phenomena that in principle could lead to the enhanced qr-satellite emission due to an ionization abundance, which is lacking beyond the electron temperature. However, taking the transient numerical data for a Lagrangian cell from gasdynamical calculations (see Fig. 7), we find that in the early stage of plasma development (corresponding to spectra near the target surface to which we confine our present discussion), these effects are small. The main reason for this is the high electron density in the first few ns after the target ablation driving the confinement parameter ($n_e\tau$) to large values. The detailed non-Maxwellian investigation of the data with the MARIA-simulations showed that T_{cold} is rather low, about 60 eV, while the temperature of hot electrons T_{hot} is about 1 keV (or higher). The reasons are as follows. Usually the hot electron component not only increases inner-shell excitation rates (and therefore rises the corresponding lines, e.g., the qr-satellites), but also drives the ionic population to higher-charge states through increased ionization rates. In quasi-stationary plasmas with the confinement parameters

$$n_e\tau \geq 10^{12} \text{ cm}^{-3} \cdot \text{s}, \tag{14}$$

the increased inner-shell excitation rates and depleted charge states can partly cancel. However, if the bulk electron temperature is very low, we meet with an entirely different regime: the hot electrons are not able to shift the ionic charge states to significantly higher values and increased inner-shell excitation rates are directly visible through the increased emission of the corresponding lines. In this regime, the spectroscopic diagnostic is extremely sensitive to the hot electron fraction and the low values of f_{hot} about 10^{-6} lead to

significant changes in the spectral distribution. This is shown in Fig. 9 for the intercombination line $He_{\alpha 2}$, qr- and kj-satellites. Two important observations can be made from this figure: first, the critical value of kT_{cold}, where the influence of the hot electrons starts to be essential, is different for different lines (see arrows), second, the «bumps» for curves (b) are also very different. In particular, the bump for the qr-satellites at about $kT_{cold} \approx 50$ eV is so strongly pronounced that it even leads to a local maximum (the increased inner-shell excitation rates strongly dominate over the shifted balance, see the discussion above). Therefore, the qr-satellites rise in intensity relative to the other emission lines. The different threshold values (in particular, those for the kj-satellites) have the following origin: the dielectronic capture energy and the excitation energy for the intercombination line are different. The small bump for the kj-satellites results from the dielectronic recombination caused by the distribution function with the parameter kT_{hot}. These overall characteristics are caused by the excitation from different channels through different mechanisms: the inner-shell excitation for the qr-satellites, collisional excitation from the He-like ground state for the intercombination line, and dielectronic capture into the He-like ground state for the kj-satellites. Precisely these different channels make the selected emission lines suitable for the hot electron investigation.

Figure 8b also shows the theoretical fitting of the experimental spectrum. The theoretical spectrum was obtained for $kT_{cold} = 60$ eV, $n_e = 10^{19}$ cm^{-3}, $kT_{hot} = 1$ keV, $f_{hot} = 4 \cdot 10^{-7}$, and $L_{eff} = 500$ μm. It should be noted that it was impossible to describe the relative structure of satellite lines without introducing hot electrons. On the other hand, it is impossible to explain the blue wing of the $He_{\alpha 2}$ line without the introduction of fast ions. The relative structure of satellite intensities is not very sensitive to the hot electron energy if T_{hot} is comparable to or larger than the threshold value (because the rate coefficients are mainly inversely proportional to the square root of T_{hot} and do not show a strong exponential dependence). Therefore, T_{hot} may be significantly higher.

We next consider spatial non-uniformity of the plasmas. In Fig. 10, we present the spatial distribution of plasma parameters (at the time of the peak laser intensity) from the simulation of the CO_2 laser-produced plasma. Figure 10a shows the electron density as a function of radius together with the population densities of Li-like and He-like Mg. It is easily seen that Li-like ions are present only in a rather narrow spatial region of about 20 μm, while the He-like Mg ions occupy an order of magnitude wider region. Figure 10b shows the distribution of the electron temperature and Fig. 10c presents the distribution of the radiation power density (per unit volume) for the He-like resonance (R) and intercombination (I) lines. Two things are important to emphasize. First, resonance and intercombination lines of He-like magnesium have a peak of the radiation power at an electron density much higher than critical. This explains the rather large X-ray emission intensity fixed in experiments. Second, the electron temperature at the point where the peak of these two lines occurs is about 200 eV, which is significantly higher than the temperature at the point where the peak of Li-like Mg is situated (60 eV). From these results, we conclude that the emission of the He-like resonance line and associated satellite lines originate from two distinct regions in which both the temperature and electron density are quite different. The fact that the resonance line and the satellites are radiated from different spatial regions is valid for lower and higher laser radiation intensities (we performed simulations in the

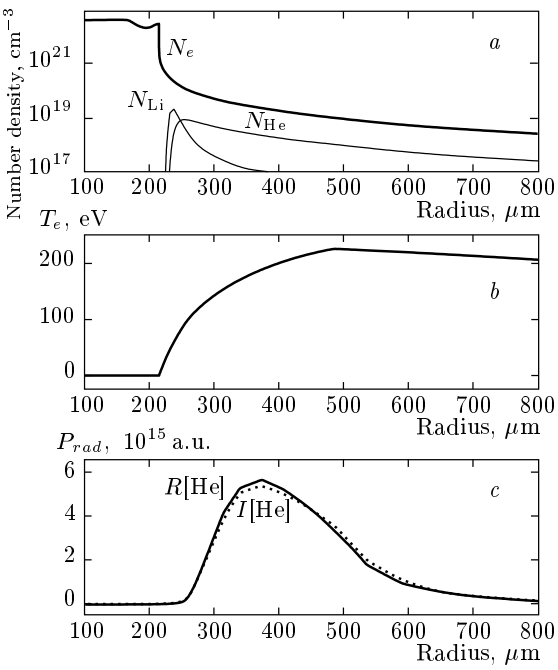

Fig. 10. The calculated distribution of plasma parameters for a spherically-symmetric target irradiated by the CO_2 laser pulse: a — electron density (N_e) and number densities of Li-like and He-like magnesium ($N_{\rm Li}$ and $N_{\rm He}$ respectively) along the radius; b — the electron temperature T_e, c — the radiation power density of the resonance and intercombination lines of He-like magnesium (R[He] and I[He] respectively)

range of intensities $P_0 = 5 \cdot 10^{11}$–$1 \cdot 10^{14}$ W/cm^2) as well as for plasma parameters corresponding to the peak of the Li-like ion abundance. The peak of the He-like resonance line is found to be very conservative against changes of the laser power density.

The presence of blue wings at the He-like resonance and intercombination lines and the absence of this feature on satellites also indicates that satellites are radiated from narrow regions where the velocity does not change significantly. On the other hand, the resonance line is radiated from a rather wide region where the plasma is strongly accelerated.

Taking the plasma non-uniformity into account, we treat the effective electron temperature obtained by comparing the intensities of both He-like and Li-like transitions as, probably, strongly underestimated in comparison to the peak electron temperature. Because we revealed that the He-like resonance line is insensitive to the density fraction of hot electrons (for $f \leq 10^{-5}$ at least) at the electron temperatures above $T_e = 120$ eV the value of f obtained by the spectrum fitting is probably also underestimated. Nevertheless, the sensitivity of the method to the density of hot electrons is surprisingly high.

6. NON-UNIFORM LASER INTENSITY DISTRIBUTION WITHIN THE FOCAL SPOT

One of the important features of our experiments was a strong non-uniformity of the laser intensity distribution within the focal spot at the «nhelix» and TIR-1 lasers. At the «nhelix» laser facility, this distribution was measured. Results presented in Fig. 11 demonstrate the complex structure of the laser intensity distribution.

Under the conditions of experiments at the TIR-1 laser facility, the intensity pattern was also not uniform (due to the shifts of targets away from the optimal focus). The two-dimensional laser intensity distribution was obtained from numerical simulation performed with the FOCUS code for the real experimental geometry. FOCUS is a two-dimensional diffraction code for the calculation of light intensity distribution in complex optical schemes that can include an arbitrary number of apertures of arbitrary shape and plane or spherical mirrors. The concentric gap appears due to the shadow of the target and the support pivot placed into the converging light beam. Diffraction of the laser beam on the target introduces additional peaks. In our view, these quite non-uniform intensity distribution patterns provoke filamentation of laser light, which leads to the

Fig. 11. The measured laser intensity distribution in the focal spot at the «nhelix» laser facility

Fig. 12. The X-ray pinhole image of Mg plasmas produced by CO_2 TIR-1-laser at the intensity $6 \cdot 10^{12}$ W/cm^2 (average over 10 shots). Three plasma jets (see arrows) originate from the hot spot

creation of locally overheated regions. This effect in the CO_2 laser-produced plasma was, probably, first reported in [42], where the filamentation effect was observed above the incident intensity $\sim 2 \cdot 10^{12}$ W/cm^2, a value being essentially lower than in our experiments at TIR-1. At the same time, our pinhole images produced by several subsequent shots (from four to ten) clearly demonstrate several «plasma jets» (see arrows in Fig. 12), which, would be averaged on the film in the case of stochastic filamentation. The example of an X-ray pinhole image is shown in Fig. 12. This qualitatively proves the presumed correlation of the laser intensity non-uniformity and the appearance of laser light filamentation, which, as a consequence, leads to an «easier» generation of fast ions and electrons. This might be a way to control the fast particle production, but in the present work, we did not aim at any optimizations.

Our experiments demonstrate that the generation of fast electrons and ions can be achieved at very low levels of laser intensity compared to that reached at femtosecond lasers [43, 44] ($q\lambda^2 > 10^{18}$ W·μm^2/cm^2). As Fig. 5 indicates, fast ion energy shows no clear correlation with the $q\lambda^2$ parameter. This is in line with the observation of the fast ion generation in the CO_2 laser-produced plasma, which was significantly less efficient than when we studied plasmas created by lasers in the visible wavelength range (while one would expect the opposite due to much lower critical electron density).

7. CONCLUSIONS

We have studied the fast ion and hot electron production at various different laser installations at GSI-Darmstadt (Germany), Saclay (France), Frascati (Italy) and TRINITI (Russia) for Nd-Glass, Ti-Sapphire, XeCl, and CO_2 lasers by means of high-resolution X-ray spectroscopic methods and ion-time-of-flight measurements. The spectroscopic approach provides information about the plasma particles even inside the plasma volume. Experimentally further advantageous is the fact that the analysis is based on a unique footing, namely on the investigation of a highly resolved spectral interval containing numerous X-ray line transitions of target ions from states with various charges.

Fast ion distributions have been characterized through Doppler-shifted line wings of spatially resolved X-ray spectra originating from highly charged target ions inside the plasma volume. For laser intensities $q\lambda^2 < 10^{14}$ W·μm^2/cm^2, a large scattering (by orders of magnitude) of fast ion energies have been obtained. These observations are presumably caused by inhomogeneous intensity distributions over the laser spot, which have been identified with measurements and two-dimensional diffraction calculations. These scatters might be advantageous for a simple creation of MeV-energy ions with sufficiently low laser intensities: in fact, MeV-energy ions for relatively low intensities $q\lambda^2 < 10^{13}$ W·μm^2/cm^2 have been observed.

MHD and non-Maxwellian spectroscopy have been used to characterize plasmas containing non-Maxwellian particles. Methods were developed to determine the electron bulk-temperature and the hot electron fraction with the sensitivity down to about 10^{-5} (compared to the electron bulk). These methods are based on the detailed analysis of the spectral distribution of the radiation emission of multi-excited target ions near the target surface.

This work was partly supported by INTAS (project 97-2090).

REFERENCES

1. *PHELIX, Petawatt High-Energy Laser for Heavy-Ion Experiments*, GSI-98-10, Report (1998).
2. F. B. Rosmej, U. N. Funk, M. Geißel et al., JQSRT **65**, 477 (2000).
3. J. Lindl, Phys. Plasmas **2**, 3934 (1995).
4. S. J. Gitomer, R. D. Jones, F. Begay et al., Phys. Fluids **29**, 2679 (1986).
5. Laser and Particles Beams, ed. by B. Yu. Sharkov (1996), Vol. 24, № 3.
6. V. A. Boiko, O. N. Krokhin, S. A. Pikuz, A. Ya. Faenov, and A. Yu. Chugunov, Sov. J. Plasma Phys. **1**, 165 (1975).
7. N. G. Basov, S. V. Bobashev, K. Gotz, M. P. Kalashnikov et al., Pis'ma v Zh. Eskp. Teor. Fiz. **36**, 229 (1982).
8. F. B. Rosmej, D. H. H. Hoffmann, W. Süß et al., Pis'ma v Zh. Eskp. Teor. Fiz. **70**, 270 (1999).
9. S. Dobosz, M. Schmidt, M. Perdrix et al., Pis'ma v Zh. Eskp. Teor. Fiz. **68**, 485 (1998).
10. A. G. Zhidkov, A. Sasaki, T. Tajima et al., Phys. Rev. E **60**, 3273 (1999).
11. S. Bollanti, P. Di Lazarro, F. Flora et al., Physica Scripta **51**, 326 (1995).

12. V. Yu. Baranov, K. N. Makarov, V. C. Roerich et al., Laser and Particles Beams **14**, 347 (1996).

13. I. Yu. Skobelev, A. Ya. Faenov, B. A. Bryunetkin et al., Zh. Eskp. Teor. Fiz. **108**, 1263 (1995).

14. B. K. F. Young, A. L. Osterheld, D. F. Price et al., Review of Scientific Instrum. **69**, 4049 (1998).

15. P. Wägli and T. P. Donaldson, Phys. Rev. Lett. **40**, 875 (1978).

16. M. Schnürer, M. P. Kalashnikov, P. Nickles et al., Phys. Plasmas **2**, 3106 (1995).

17. P. Wägli, T. P. Donaldson, and P. Lädrach, Appl. Phys. Lett. **32**, 638 (1978).

18. B. C. Boland, F. E. Irons, and R. W. P. McWhirter, J. Phys. B **1**, 1180 (1968).

19. C. Fauquignon and F. Floux, Phys. Fluids **13**, 386 (1970).

20. M. Waki, T. Yamanaka, H. Kang, K. Yoshida, and C. Yamanaka, Jap. J. Appl. Phys. **11**, 420 (1972).

21. Los Alamos National Lab. Report № LA-UR 76-2242 (1976).

22. K. Dick and H. Pepin, Opt. Commun. **13**, 289 (1975).

23. C. Yamanaka, T. Yamanaka, T. Sasaki, and J. Mizui, Phys. Rev. Lett. **32**, 1038 (1974).

24. E. Fabre, C. Garban, C. Popovics et al., in *Plasma Physics and Controlled Nuclear Fusion Research*, IAEA, Vienna (1975), Vol. II, p. 597.

25. H. Pepin, B. Grek, F. Rhealt, and D. Nagel, J. Appl. Phys. **48**, 3312 (1977).

26. A. E. Stepanov, A. N. Starostin, V. C. Roerich et al., JQSRT **58**, 937 (1997).

27. G. B. Rybicki and D. G. Hummer, Astrophys. J. **274**, 380 (1983).

28. F. B. Rosmej, J. Phys. B Lett. **30**, L819 (1997).

29. F. B. Rosmej, A. Ya. Faenov, T. A. Pikuz et al., Pis'ma v Zh. Eskp. Teor. Fiz. **65**, 708 (1997).

30. F. B. Rosmej, A. Ya. Faenov, T. A. Pikuz et al., JQSRT **58**, 859 (1997).

31. F. B. Rosmej, D. Reiter, V. S. Lisitsa et al., Plasma Physics and Controlled Fusion **41**, 191 (1999).

32. D. W. Forslund and J. U. Blackbill, Phys. Rev. Lett. **48**, 1614 (1982).

33. N. E. Andreev, Yu. A. Zakharenkov, N. N. Zorev et al., Zh. Eskp. Teor. Fiz. **70**, 547 (1976).

34. A. S. Shlyaptseva, A. M. Urnov, and A. V. Vinogradov, Preprint FIAN № 193, Moscow (1981).

35. M. K. Inal and J. Dubau, J. Phys. B **22**, 3329 (1989).

36. F. B. Rosmej, JQSRT **51**, 319 (1994).

37. F. B. Rosmej and O. N. Rosmej, AIP **299**, 560 (1994).

38. F. B. Rosmej, J. Phys. B Lett. **28**, L747 (1995).

39. J. Jr. Abdallah, A. Ya. Faenov, D. Hammer et al., Physica Scripta **53**, 705 (1996).

40. J. P. Matte, J. C. Kieffer, S. Ethier, and M. Chaker, Phys. Rev. Lett. **53**, 1461 (1994).

41. A. H. Gabriel, Mon. Not. R. Astro. Soc. **160**, 99 (1972).

42. T. P. Donaldson and I. J. Spalding, Phys. Rev. Lett. **36**, 467 (1976).

43. P. Gibbon and E. Forster, Plasma Phys. Control. Fusion **38**, 759 (1996).

44. A. G. Zhidkov, A. Sasaki, T. Tajima et al., Phys. Rev. E **60**, 3273 (1999).